CrossMark

Two Intermediate-mass Transiting Brown Dwarfs from the TESS Mission

Theron W. Carmichael[1,2,20], Samuel N. Quinn[2], Alexander J. Mustill[3], Chelsea Huang[4], George Zhou[2],
Carina M. Persson[5], Louise D. Nielsen[6], Karen A. Collins[2], Carl Ziegler[7], Kevin I. Collins[8], Joseph E. Rodriguez[2],
Avi Shporer[4], Rafael Brahm[9,10], Andrew W. Mann[11], Francois Bouchy[6], Malcolm Fridlund[5,12], Keivan G. Stassun[13,14],
Coel Hellier[15], Julia V. Seidel[6], Manu Stalport[6], Stephane Udry[6], Francesco Pepe[6], Michael Ireland[16], Maruša Žerjal[16],
César Briceño[17], Nicholas Law[11], Andrés Jordán[9,10], Néstor Espinoza[18], Thomas Henning[19], Paula Sarkis[19], and
David W. Latham[2]

[1] Department of Astronomy, Harvard University, Cambridge, MA 02138, USA; tcarmich@cfa.harvard.edu
[2] Center for Astrophysics, Harvard & Smithsonian, 60 Garden Street, Cambridge, MA 02138, USA
[3] Lund Observatory, Department of Astronomy and Theoretical Physics, Lund University, Box 43, SE-221 00 Lund, Sweden
[4] Department of Physics, and Kavli Institute for Astrophysics and Space Research, Massachusetts Institute of Technology, Cambridge, MA 02139, USA
[5] Chalmers University of Technology, Department of Space, Earth and Environment, Onsala Space Observatory, SE-439 92 Onsala, Sweden
[6] Geneva Observatory, University of Geneva, Chemin des Mailettes 51, 1290 Versoix, Switzerland
[7] Dunlap Institute for Astronomy and Astrophysics, University of Toronto, 50 St. George Street, Toronto, Ontario M5S 3H4, Canada
[8] George Mason University, 4400 University Drive, Fairfax, VA 22030, USA
[9] Facultad de Ingeniería y Ciencias, Universidad Adolfo Ibáñez, Av. Diagonal las Torres 2640, Peñalolén, Santiago, Chile
[10] Millennium Institute for Astrophysics, Chile
[11] Department of Physics and Astronomy, The University of North Carolina at Chapel Hill, Chapel Hill, NC 27599-3255, USA
[12] Leiden Observatory, University of Leiden, P.O. Box 9513, 2300 RA, Leiden, The Netherlands
[13] Vanderbilt University, Department of Physics & Astronomy, 6301 Stevenson Center Lane, Nashville, TN 37235, USA
[14] Fisk University, Department of Physics, 1000 18th Avenue N., Nashville, TN 37208, USA
[15] Astrophysics Group, Keele University, Staffordshire, ST5 5BG, UK
[16] Research School of Astronomy and Astrophysics, The Australian National University, ACT, 2611, Australia
[17] Cerro Tololo Inter-American Observatory, Casilla 603, La Serena, Chile
[18] Space Telescope Science Institute, 3700 San Martin Drive, Baltimore, MD 21218, USA
[19] Max-Planck-Institut für Astronomie, Königstuhl 17, Heidelberg D-69117, Germany

Abstract

We report the discovery of two intermediate-mass transiting brown dwarfs (BDs), TOI-569b and TOI-1406b, from NASA's Transiting Exoplanet Survey Satellite mission. TOI-569b has an orbital period of $P = 6.55604 \pm 0.00016$ days, a mass of $M_b = 64.1 \pm 1.9\ M_{\rm J}$, and a radius of $R_b = 0.75 \pm 0.02\ R_{\rm J}$. Its host star, TOI-569, has a mass of $M_\star = 1.21 \pm 0.05\ M_\odot$, a radius of $R_\star = 1.47 \pm 0.03\ R_\odot$, [Fe/H] $= +0.29 \pm 0.09$ dex, and an effective temperature of $T_{\rm eff} = 5768 \pm 110$ K. TOI-1406b has an orbital period of $P = 10.57415 \pm 0.00063$ days, a mass of $M_b = 46.0 \pm 2.7\ M_{\rm J}$, and a radius of $R_b = 0.86 \pm 0.03\ R_{\rm J}$. The host star for this BD has a mass of $M_\star = 1.18 \pm 0.09\ M_\odot$, a radius of $R_\star = 1.35 \pm 0.03\ R_\odot$, [Fe/H] $= -0.08 \pm 0.09$ dex, and an effective temperature of $T_{\rm eff} = 6290 \pm 100$ K. Both BDs are in circular orbits around their host stars and are older than 3 Gyr based on stellar isochrone models of the stars. TOI-569 is one of two slightly evolved stars known to host a transiting BD (the other being KOI-415). TOI-1406b is one of three known transiting BDs to occupy the mass range of 40–50 $M_{\rm J}$ and one of two to have a circular orbit at a period near 10 days (with the first being KOI-205b). Both BDs have reliable ages from stellar isochrones, in addition to their well-constrained masses and radii, making them particularly valuable as tests for substellar isochrones in the BD mass–radius diagram.

Unified Astronomy Thesaurus concepts: Brown dwarfs (185); Radial velocity (1332); Transit photometry (1709); Spectroscopy (1558); Photometry (1234); Substellar companion stars (1648)

1. Introduction

Brown dwarfs (BDs) are traditionally defined as objects with masses between 13 and 80 Jupiter masses ($M_{\rm J}$) and, for those that orbit main-sequence stars, are typically observed to be 0.7 to 1.4 Jupiter radii ($R_{\rm J}$) in size (Csizmadia & CoRot Team 2016; Carmichael et al. 2019). The lower mass limit that separates planets from BDs corresponds to the threshold required to fuse deuterium in the core of the BD, which, in detail, is $11-16\ M_{\rm J}$, depending on the metallicity of the BD (Spiegel et al. 2011). The threshold to fuse hydrogen in the core is $75-80\ M_{\rm J}$, and this separates BDs from stars. This higher threshold depends on the initial formation conditions and how convection affects the object (Baraffe et al. 2002). The mass and radius of a BD are

measured through a combination of observational techniques, with the most important being radial velocity (RV) measurements and transit photometry of the host star.

This is where the Transiting Exoplanet Survey Satellite (TESS) mission plays a major role. The transit method has been most successful in the characterization of BDs in relatively short orbital periods (on the order of 10–20 days or less to detect multiple transits), which is why the TESS mission has been particularly useful in making the initial detections of recently discovered transiting BDs (e.g., Jackman et al. 2019; Subjak et al. 2020). The transit light curves from TESS are taken over roughly 28 consecutive days per sector (or up to 1 year for overlapping sectors), with occasional gaps in coverage due to data downloads and instrumental anomalies. These light curves give an estimate of the radius of the candidate companions relative to the radius of the star. This provides us with information about whether or not a

_____
[20] National Science Foundation Graduate Research Fellow.

candidate companion is within the typical range of radii expected for a BD orbiting a main-sequence star. We are particularly fortunate at the present time to be able to utilize the parallax measurements from Gaia DR2 (Gaia Collaboration et al. 2018) to derive precise stellar distances and radii for stars that host transiting BDs.

Though TESS and Gaia provide us with some handle on the radius of a BD, follow-up spectra are needed to accumulate a series of RV measurements to determine an orbit and measure a mass. This is an important step, as objects ranging from roughly 1 M_J to 100 M_J may have the same radius (∼1 R_J), so the only way to distinguish them is through a mass measurement. Since the masses of transiting BDs produce large RV signals around typical FGK main-sequence stars, RV follow-up of these BDs is fairly accessible (especially given the precision of modern echelle spectrographs).

When comparing the detection of transiting BDs to the detection of transiting giant planets, we see two facts emerge: (1) for host stars with similar radii, transiting BDs should be roughly as easy to detect as hot Jupiters, given both types of objects are similar in size and given the photometric precision and sensitivity of transit survey missions like TESS; (2) for host stars of similar masses, it is as easy or easier to characterize the mass of a BD, given that they are more massive and produce larger RV signals than giant planets. Despite this, we know of only 23 transiting BDs (see Table 7 for a list). When compared to the number of known transiting hot Jupiters and even eclipsing low-mass stellar companions in comparable orbital periods, it is easy to see that there is a lack of transiting BDs; this is the so-called brown dwarf desert (Marcy & Butler 2000). Though not yet clear, this "desert" may result from the distributions of the two different formation mechanisms (one for planets and one for stars) tailing off—and perhaps overlapping—somewhere within the nominal BD mass range.

To understand this population on a deeper level, we use the mass, radius, and age of transiting BDs to examine how these substellar objects evolve compared to substellar evolutionary models (e.g., Baraffe et al. 2003). Since a BD may only fuse deuterium and not hydrogen, it lacks the energy source needed to stave off gravitational contraction on long timescales as effectively as stars do, so the BD's radius will shrink as it ages. This is why the age is important in addition to mass and radius. If we can reliably determine the age of a star that hosts a transiting BD, whether through an association with a star cluster, gyrochronology, or asteroseismology, then we may use that transiting BD to test substellar evolutionary models in mass, radius, and age parameter spaces. This assumes that both the host star and the transiting BD form at the same time. So far, only three BDs transiting main-sequence stars with well-determined ages are known (Gillen et al. 2017; Beatty et al. 2018; David et al. 2019), so we are lacking test points on the substellar mass–radius diagram with precisely determined mass, radius, and age.

Here we report the discovery and characterization of two new transiting BDs with reliable mass, radius, and age measurements: TOI-569b and TOI-1406b. TOI-569b orbits a recently evolved star in a circular orbit. TOI-1406b orbits an F-type star, joining seven other transiting BDs that orbit F-type stars, and is also in a circular orbit. These both serve as new test points on the mass–radius diagram for BDs older than 3 Gyr. In Section 2, we provide details on the light curves and spectra

Table 1
Coordinates and Magnitudes for TOI-569 and TOI-1406

	Description	TOI-569	TOI-1406	Source
α_{J2000}	Equatorial	07 40 24.67	05 28 30.71	1
δ_{J2000}	Coordinates	−42 09 16.79	−48 24 32.64	1
T	TESS T	9.473 ± 0.006	11.427 ± 0.006	2
G	Gaia G	9.936 ± 0.001	11.759 ± 0.001	1
B_T	Tycho B_T	11.036 ± 0.048	13.352 ± 0.359	3
V_T	Tycho V_T	10.173 ± 0.032	12.074 ± 0.195	3
J	2MASS J	8.829 ± 0.020	10.929 ± 0.020	4
H	2MASS H	8.575 ± 0.060	10.787 ± 0.030	4
K_S	2MASS K_S	8.444 ± 0.020	10.675 ± 0.020	4
WISE1	WISE 3.4 μm	8.419 ± 0.023	10.649 ± 0.023	5
WISE2	WISE 4.6 μm	8.467 ± 0.020	10.692 ± 0.021	5
WISE3	WISE 12 μm	8.414 ± 0.021	10.651 ± 0.062	5
WISE4	WISE 22 μm	8.180 ± 0.188	⋯	5

Note. The values here make up the spectral energy distributions used to model the stars.
References. (1) Lindegren et al. (2018), corrected from the J2015 epoch, (2) Stassun et al. (2018b), (3) Høg et al. (2000), (4) Skrutskie et al. (2006), (5) Wright et al. (2010).

that were obtained for this study, with additional attention given to the determination of the orbital period of TOI-569b, which was initially reported incorrectly as twice its actual value due to gaps in the TESS data. Section 3 describes the analysis techniques used to derive the host star and BD properties. Section 4 discusses the implications of these discoveries in the BD mass–radius diagram, as these two transiting BDs are the oldest transiting BDs that have been well-characterized.

2. Observations

2.1. TESS and Ground-based Light Curves

The light curves of TOI-569 come from the TESS mission, in sectors 7 and 8, and the Las Cumbres Observatory (LCOGT). For the TESS light curve for TOI-569, we use the Pre-search Data Conditioning Simple Aperture Photometry flux (PDCSAP; Smith et al. 2012; Stumpe et al. 2014) from the Mikulski Archive for Space Telescopes (MAST).[21] The PDCSAP light curve has systematic effects removed, and with this, we then normalize the light curve with the `lightkurve` package in Python (the Lightkurve Collaboration et al. 2018). The light curves used for TOI-1406 come from the full-frame images (30 minutes cadence) from the TESS mission in sectors 4, 5, and 6. We use the `lightkurve` package to extract and normalize the light curve of TOI-1406. Coordinates and magnitudes for TOI-569 and TOI-1406 are given in Table 1.

For the light-curve extraction, we use circular apertures that are fixed to the target star's position for each sector. When the star moves slightly between sectors, the aperture is moved to follow it. The counts from each pixel within the aperture are summed, and the resulting light curve is detrended using the `lightkurve` package's built-in flattening tool, which we use to remove stellar rotational variability, when present, as well as scattered background light. The detrended TESS light curves are shown in Figure 1.

We observed an ingress of TOI-569 continuously for 140 minutes on 2019 April 15 using 15 s exposures and a z-short
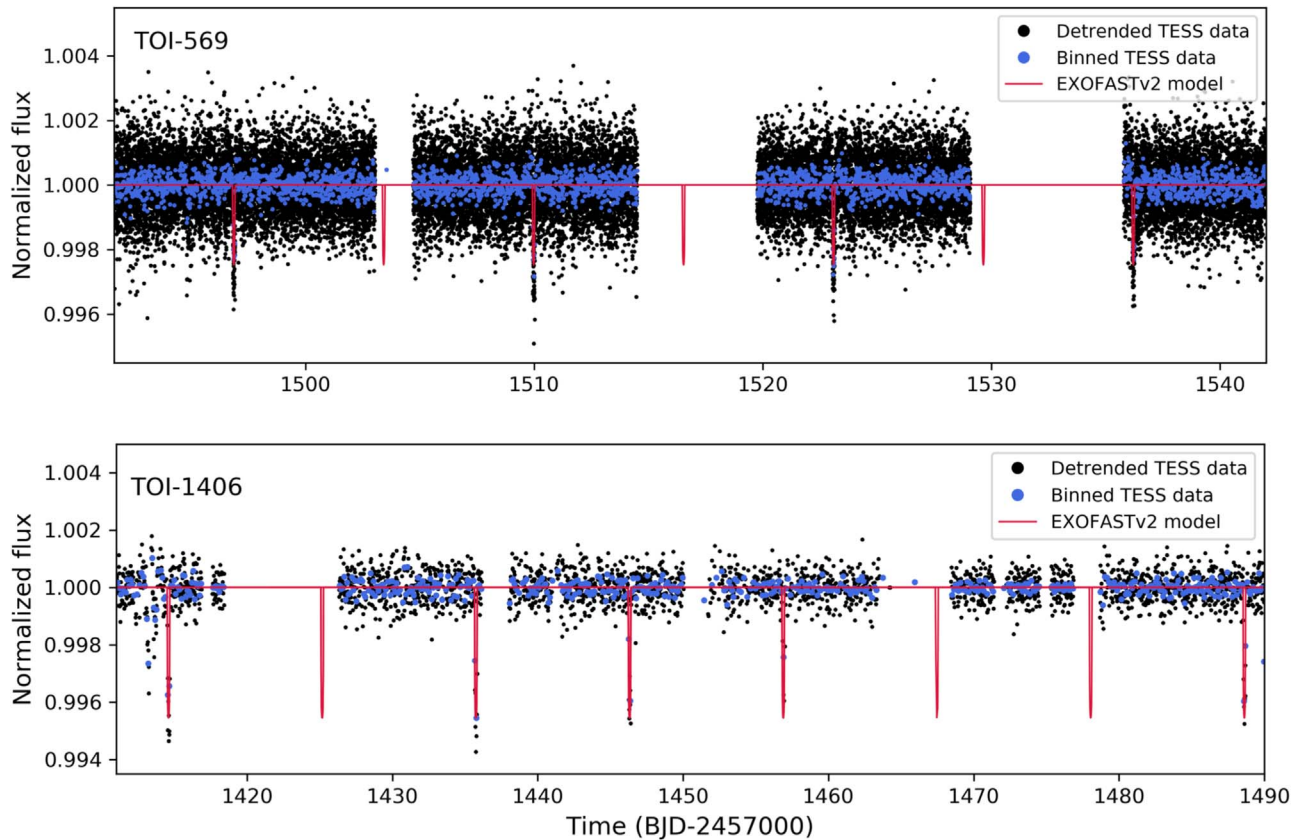
---

[21] https://mast.stsci.edu/portal/Mashup/Clients/Mast/Portal.html

Figure 1. Top: detrended TESS light curve of TOI-569 in the black points. The star was observed at 2 minutes cadence in TESS sectors 7 and 8, and the binning shown here as blue points uses bin sizes of 45 minutes. This star also exhibits periodic 1%–3% flux variations, likely due to star spots based on the changes in the patterns of the modulation; these effects have been removed for the transit analysis. Bottom: detrended TESS light curve of TOI-1406 (black points) obtained from the full-frame images at 30 minutes cadence from TESS sectors 4, 5, and 6, with the bin sizes at a length of 90 minutes (blue points).

band filter from the LCOGT (Brown et al. 2013) 1.0 m node at Cerro Tololo Inter-American Observatory. We used the TESS Transit Finder, which is a customized version of the Tapir software package (Jensen 2013), to schedule our transit observations. The 4096 × 4096 LCOGT SINISTRO cameras have an image scale of 0″.389 per pixel, resulting in a 26′ × 26′ field of view. The images were calibrated by the standard LCOGT BANZAI pipeline, and photometric data were extracted with the AstroImageJ software package (Collins et al. 2017) using a circular aperture with radius 5″.8. The images have typical stellar point-spread-functions with a half-width-half-maximum of 1″. We detect a ∼3000 ppm ingress on target with apertures as small as 2″ in radius. Systematic effects start to dominate the light curve for smaller apertures. Thus, we confirm that the source of the TESS detection is within 3″ of the target star location and that the transit depth from the LCOGT partial transit is consistent with the TESS depth for all aperture radii we checked down to 2″. We did not obtain any ground-based photometric follow-up of TOI-1406.

2.1.1. Light Curve Modulation and the Orbital Period of the TOI-569 System

Previous to the transit detections of TOI-569b from TESS, the Wide Angle Search for Planets (WASP) found a 13-day modulation in the light curve of TOI-569. The phased light curve for WASP is shown in Figure 2. The WASP data were taken during the 2011–2012 seasons, with a 150-day span of

coverage. The transits of TOI-569b are too shallow to be detected in the WASP light curve, even when phase folded to the ephemeris from TESS, but they can be seen in the TESS light curve in the top panel of Figure 2. The WASP and TESS light curves show a similar but not exactly equal modulation. The periodic peaks and dips in both light curves are likely from brightness variations due to star spots, which are known to vary over time. The unevenness in the peaks in the TESS light curves is likely from multiple different starspot configurations on different areas on the surface of the star, in addition to the evolution of spot brightness over time.

The gaps in the TESS light curve occur during every other transit of TOI-569b in the sectors where the host star was observed. This is the reason why the initial orbital period was reported to be 13.12 days (twice the true orbital period of 6.56 days). We discovered that this was the case, as the orbital solution developed with RV follow-up using the instruments described in later sections. It seems coincidental that this erroneous orbital period of 13.12 days is nearly equal to the 13 days modulation in the WASP light curve. This made the BD appear to have an orbit synchronized with the rotation rate of the star, but this turned out not to be the case upon a more thorough investigation that accounts for the orbital solution derived from RVs. We note that the observation of the transit of TOI-569b with the LCOGT 1 m telescope did not occur at opposite parity to the transits detected by TESS, so we cannot use this to independently confirm the 6.56 days period of TOI-569b.
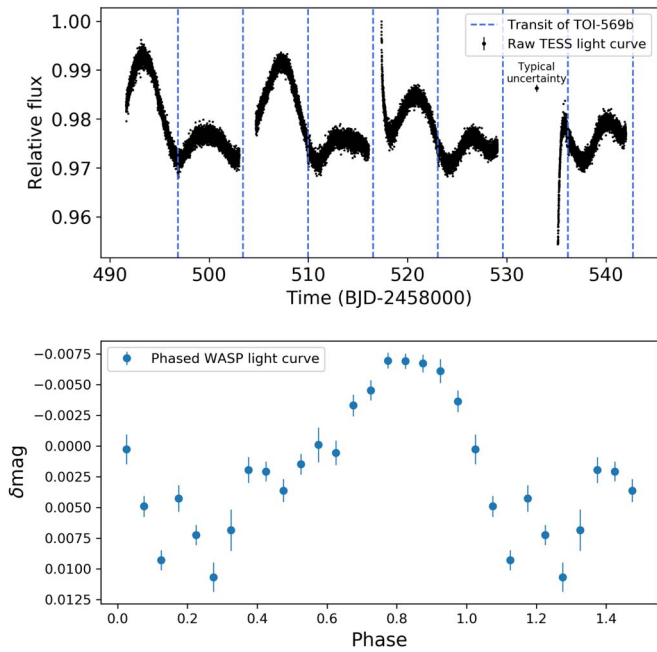
Figure 2. Top: offset-normalized raw TESS light curve from sectors 7 and 8 of TOI-569. The offset between each sector is removed using `lightkurve`, but no other systematic effects are removed since the focus of this figure is to show the missed transits of TOI-569b and provide context for the flux variability of the host star. The rapid ramp down at 515 days and ramp up at 535 days are instrumental systematics from the spacecraft. The blue dashed lines show the transit times predicted by the final model ephemeris for TOI-569b. Bottom: WASP light curve of TOI-569 phase folded at 13.03 days from observations taken over a span of 150 days.

Figure 3. Top: Lomb–Scargle periodogram from the TESS light curve of TOI-569. Bottom: Lomb–Scargle periodogram from the WASP light curve of TOI-569. Both the WASP and TESS periodograms indicate a peak frequency near 13 days. The peak in the lower panel is narrower because the total time coverage from the WASP data was nearly three times longer than that from TESS.

Using a Lomb–Scargle periodogram analysis on both the TESS and WASP light curves separately (Figure 3), we see a peak frequency at roughly 13 days (12.91 days for TESS and 13.01 days for WASP). This may suggest that TOI-569 and its companion BD are in a 2:1 spin–orbit resonance.

2.2. High-resolution Imaging and Contaminating Sources

Though the LCOGT data give us a sense of whether or not the transit signals for TOI-569 are within roughly $3''$ of the target star, we may use speckle imaging to confirm whether or not there is contamination even closer to the target. For TOI-569, we used SOAR speckle imaging to look for other objects within the TESS aperture that would significantly contaminate the transit and RV signals we observe. Nearby stars that fall within the same TESS image profile as the target can cause photometric contamination or be the source of an astrophysical false positive, such as a background or nearby eclipsing binary star. We searched for nearby sources to TOI-569 with SOAR speckle imaging (Tokovinin 2018) on 2019 May 18, observing in a similar visible bandpass as TESS (the Cousins-I-band). Further details of the observations are available in Ziegler et al. (2020). We detected no nearby stars within $3''$ of TOI-569. The 5σ detection sensitivity and the speckle auto-correlation function from the SOAR observation are plotted in Figure 4.

We also use data from Gaia DR2 (Gaia Collaboration et al. 2018) to gather a census of nearby stars, finding that no stars brighter than $G = 17.0$ are within $25''$ and only two stars with $G = 13.7$ and $G = 14.9$ are approximately $26''$ from TOI-569, which has a brightness of $G = 9.9$ (Table 2). These other fainter stars also do not share the same proper motion as
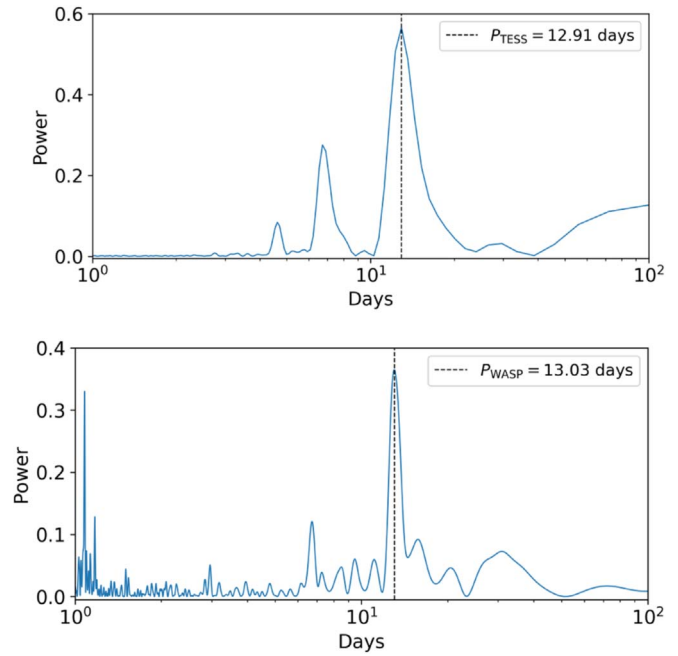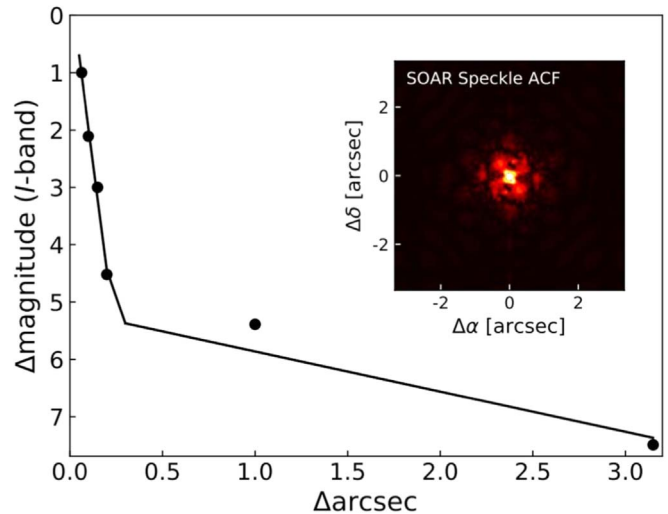

Figure 4. 5σ sensitivity limits and auto-correlation functions of the SOAR speckle observations of TOI-569. The black circles are measured data points, and the lines are fits in two different separation regimes. In general, the sensitivity of speckle imaging to companions rises sharply from the diffraction limit to a "knee" at a separation of $0''.15$–$0''.2$, where it then continues to slowly increase out to $1''.5$, beyond which the speckle patterns begin to become de-correlated. No nearby contaminating sources are detected within $3''$.

TOI-569, which indicates that they are not associated with TOI-569 and are more distant background stars.

We do not have any high-resolution imaging (as in, sub-$3''$ coverage) for TOI-1406, but using Gaia DR2 data, we find only three other stars within $30''$ of TOI-1406. The brightest of these other stars has a magnitude of $G = 15.8$ and is $19''$ from TOI-1406, which has a magnitude of $G = 11.8$. We also find that none of these other stars share the same proper motion as TOI-1406 from the Gaia DR2 data (Table 2).

Table 2
Nearby Sources from Gaia DR2 Data

Gaia DR2 ID	α (J2000)	δ (J2000)	π (mas)	μ_α (mas yr^{-1})	μ_δ (mas yr^{-1})	G (mag)
5535473358555685760 (TOI-569)	07 40 24.67	−42 09 16.79	6.3723 ± 0.0306	6.317 ± 0.053	−3.068 ± 0.048	9.94
5535473392915426304	07 40 26.44	−42 09 00.02	0.0899 ± 0.0193	−1.790 ± 0.035	2.832 ± 0.030	13.69
5535473358555686656	07 40 23.61	−42 09 39.57	0.8838 ± 0.0275	12.130 ± 0.047	−13.344 ± 0.041	14.88
5535473358556195840	07 40 23.25	−42 09 38.38	0.1963 ± 0.0414	−4.600 ± 0.072	5.585 ± 0.060	15.64
4797030079342886784 (TOI-1406)	05 28 30.71	−48 24 32.64	2.3855 ± 0.0291	0.889 ± 0.057	−21.885 ± 0.066	11.76
4797030079342886656	05 28 29.07	−48 24 41.93	1.1846 ± 0.0396	1.222 ± 0.073	−1.752 ± 0.093	15.78

Note. This table lists sources within 30″ of each star (TOI-569 and TOI-1406) that are $G < 16$ in magnitude. Listing sources fainter than this results in too many items to reasonably list here. The parallaxes (π) and proper motions (μ_α, μ_δ) of the nearby stars indicate that none are associated with TOI-569 or TOI-1406.

2.3. CHIRON Spectra

To characterize the RVs and stellar atmospheric parameters of TOI-569 and TOI-1406, we obtained a series of spectroscopic observations using the CHIRON spectrograph on the 1.5 m SMARTS telescope (Tokovinin et al. 2013), located at Cerro Tololo Inter-American Observatory, Chile. CHIRON is a high-resolution echelle spectrograph that is fed via an image slicer and a fiber bundle. CHIRON achieves a spectral resolving power of $\lambda/\Delta\lambda \equiv R \sim 80{,}000$ over the wavelength region 4100–8700 Å. The wavelength calibration is obtained via thorium-argon hollow-cathode lamp exposures that bracket each stellar spectrum.

To derive the stellar RVs, we performed a least-squares deconvolution (Donati et al. 1997) between the observed spectra and a non-rotating synthetic template generated via ATLAS9 atmospheric models (Castelli & Kurucz 2004) at the stellar atmospheric parameters of each target. We then model the stellar line profiles derived from the least-squares deconvolution via an analytic rotational broadening kernel, as per Gray (2005). This procedure follows that done in Zhou et al. (2019). The derived RVs for TOI-569 and TOI-1406 are listed in Table 3, and this series of RVs helped reveal the true orbital period of the BD. The stellar parameters derived from the spectra of TOI-569 are $T_{\rm eff} = 5669 \pm 106$ K, $\log g = 4.11 \pm 0.18$, [Fe/H] = $+0.23 \pm 0.05$ dex, and $v \sin I_\star = 5.33 \pm 0.50$ km s^{-1}. For TOI-1406, we find $T_{\rm eff} = 6347 \pm 186$ K, $\log g = 4.09 \pm 0.15$, [Fe/H] = -0.05 ± 0.11 dex, and an approximate full width at half max for the line broadening profile of FWHM = 12.91 ± 0.24 km s^{-1} with the CHIRON spectra. For TOI-569, we take care to account for the instrumental profile and macroturbulence to extract $v \sin I_\star$ from the FWHM approximation (FWHM = 6.65 ± 0.5 km s^{-1}) with CHIRON, as this is important in our analysis of the stellar inclination in Section 3.3.

2.4. ANU 2.3 m Echelle Spectra

To help confirm TOI-1406b as a BD, we obtained six spectroscopic observations with the echelle spectrograph on the Australian National University (ANU) 2.3 m telescope, located at Siding Spring Observatory, Australia. The ANU 2.3 m echelle is a slit-fed spectrograph that yields a resolving power of $R \sim 23{,}000$ over the wavelength region of 3700–6700 Å. Wavelength calibration was provided by bracketing thorium-argon lamp exposures, and the spectra were reduced as per Zhou et al. (2014). The RVs from each exposure were measured via the least-squares deconvolution technique, as described in Section 2.3. To derive $T_{\rm eff}$, $\log g$, and [Fe/H] for TOI-1406, we use Spec-Match-emp (Yee et al. 2017), which matches the input spectra to a library of stars with well-determined parameters derived with a

variety of independent methods, such as interferometry, optical and NIR photometry, asteroseismology, and LTE analysis of high-resolution optical spectra. From the ANU spectra and Spec-Match-emp, we find $T_{\rm eff} = 6283 \pm 110$ K, $\log g = 4.13 \pm 0.12$, [Fe/H] = -0.09 ± 0.09 dex, and FWHM = 15.0 ± 1.0 km s^{-1} for TOI-1406.

2.5. CORALIE Spectra

TOI-569 was observed with the CORALIE spectrograph on the Swiss 1.2 m Euler telescope at La Silla Observatories, Chile (Queloz et al. 2001), between 2019 April 19 and May 11. CORALIE has a resolving power of $R \sim 60{,}000$ and is fed by two fibers: one 2″ diameter on-sky science fiber encompassing the star and another that can be connected to either a Fabry-Pérot etalon for simultaneous wavelength calibration or on-sky for background subtraction of the sky-flux. RVs were computed for each epoch by cross-correlating with a binary G2 mask (Pepe et al. 2002). Bisector-span, full-width half-max, and other line-profile diagnostics were computed as well, using the standard CORALIE data reduction software. Exposure times ranged from 450 to 1200 s. We obtain internal error estimates of 13–32 m s^{-1}. The resulting velocities are plotted in Figure 5 and are listed in Table 3.

The CORALIE spectra were shifted to the stellar rest frame and stacked while weighting the contribution from each spectrum with its mean flux to produce a high signal-to-noise spectrum for spectral characterization using SpecMatch-emp (Yee et al. 2017). We used the spectral region around the Mgb triplet (5100–5340 Å) to match our spectrum to the library spectra through χ^2 minimization. A weighted linear combination of the five best matching spectra was used to extract bulk stellar parameters: $T_{\rm eff} = 5481 \pm 110$ K, $\log g = 4.08 \pm 0.12$, and [Fe/H] = $+0.41 \pm 0.09$ dex for TOI-569.

2.6. FEROS Spectra

TOI-569 was observed with the FEROS spectrograph (Kaufer & Pasquini 1998) mounted on the MPG 2.2 m telescope installed at the ESO La Silla Observatory. Four spectra were obtained between 2019 April 20 and May 14. Observations were performed with the simultaneous calibration mode, where a second fiber is illuminated with a thorium-argon lamp for tracking the instrumental drift in RV during the science exposure. The adopted exposure time was of 400 s, which produced spectra with a typical signal-to-noise ratio per resolution element of 90. FEROS data were processed with the ceres pipeline (Brahm et al. 2017a), which performs the optimal extraction of the raw data, the wavelength calibration, the instrumental drift correction, and the computation of precise RVs and bisector spans. The

Table 3
Relative Radial Velocities, Bisector Span ($V_{\rm span}$), and FWHM of TOI-569 from CHIRON, CORALIE, and FEROS and of TOI-1406 from CHIRON and ANU

$\mathrm{BJD_{TDB}} - 2450000$	RV (m s^{-1})	$\sigma_{\rm RV}$ (m s^{-1})	$V_{\rm span}$ (km s^{-1})	FWHM (km s^{-1})	Instrument	Target
8594.61690	75132.3	16.6	⋯	6.93	CHIRON	TOI-569
8606.50771	77754.5	20.7	⋯	6.67	CHIRON	TOI-569
8596.60327	66265.0	18.9	⋯	7.00	CHIRON	TOI-569
8595.59076	69864.3	16.4	⋯	6.67	CHIRON	TOI-569
8607.53323	75982.6	17.8	⋯	6.73	CHIRON	TOI-569
8611.59733	71966.8	24.9	⋯	6.65	CHIRON	TOI-569
8612.57581	76679.3	30.6	⋯	6.57	CHIRON	TOI-569
8649.44500	66193.1	24.2	⋯	6.63	CHIRON	TOI-569
8651.48774	74957.8	34.9	⋯	6.81	CHIRON	TOI-569
8654.46711	70453.9	27.2	⋯	6.40	CHIRON	TOI-569
8593.58587	79347.5	13.0	−0.030	10.55	CORALIE	TOI-569
8597.47058	68533.2	31.6	0.089	10.48	CORALIE	TOI-569
8599.52446	78333.6	16.8	−0.023	10.48	CORALIE	TOI-569
8602.58567	69230.9	13.3	0.001	10.46	CORALIE	TOI-569
8603.46595	67533.0	20.3	−0.012	10.47	CORALIE	TOI-569
8614.49353	75527.3	32.4	0.004	10.43	CORALIE	TOI-569
8615.48815	70140.4	29.5	0.060	10.66	CORALIE	TOI-569
8594.49170	77148.3	6.5	0.019	⋯	FEROS	TOI-569
8595.52217	71681.8	8.4	0.015	⋯	FEROS	TOI-569
8597.51010	68686.8	6.8	0.015	⋯	FEROS	TOI-569
8617.52568	70033.1	6.0	0.009	⋯	FEROS	TOI-569
8533.07797	−19568.3	465.0	⋯	⋯	ANU	TOI-1406
8534.98787	−17679.4	197.8	⋯	⋯	ANU	TOI-1406
8536.06364	−15764.1	260.2	⋯	⋯	ANU	TOI-1406
8537.96961	−12090.1	725.7	⋯	⋯	ANU	TOI-1406
8538.93516	−12135.5	282.9	⋯	⋯	ANU	TOI-1406
8561.89365	−13798.5	270.0	⋯	⋯	ANU	TOI-1406
8540.61381	−13631.0	69.2	⋯	12.91	CHIRON	TOI-1406
8541.60193	−15950.3	91.8	⋯	12.69	CHIRON	TOI-1406
8542.56709	−17888.9	45.1	⋯	13.07	CHIRON	TOI-1406
8544.52353	−19087.2	166.4	⋯	12.78	CHIRON	TOI-1406
8546.51779	−15936.1	91.8	⋯	12.81	CHIRON	TOI-1406
8562.57958	−15177.2	126.9	⋯	12.89	CHIRON	TOI-1406
8566.55925	−18101.1	97.7	⋯	12.77	CHIRON	TOI-1406
8567.59295	−16029.1	83.6	⋯	12.82	CHIRON	TOI-1406
8568.54388	−13973.3	124.3	⋯	13.36	CHIRON	TOI-1406
8569.57364	−12432.3	110.3	⋯	12.98	CHIRON	TOI-1406

results are presented in Table 3. The four FEROS spectra were combined in order to measure the atmospheric parameters using the zaspe package (Brahm et al. 2017b), obtaining $T_{\rm eff} = 5669 \pm 80$ K, $\log g = 4.21 \pm 0.12$, [Fe/H] = +0.28 ± 0.05 dex, and an approximate FWHM = 6.45 ± 0.30 km s^{-1} for TOI-569.

3. Analysis

3.1. Modeling with EXOFASTv2

The masses and radii of the BDs are derived using EXOFASTv2. A full description of EXOFASTv2 is given in Eastman et al. (2019). EXOFASTv2 uses the Monte Carlo-Markov Chain (MCMC) method. For each MCMC fit, we use $N = 36$ ($N = 2 \times n_{\rm parameters}$) walkers, or chains, and run for 50,000 steps, or links. To derive stellar parameters, EXO-FASTv2 utilizes the MIST isochrone models (Paxton et al. 2015; Choi et al. 2016; Dotter 2016).

The parameters for which we set priors and the types of priors we set for each (i.e., uniform $\mathcal{U}[a, b]$ or Gaussian $\mathcal{G}[a, b]$) are shown for clarity. We rely on our spectroscopic measurements of [Fe/H] and $T_{\rm eff}$ and parallax measurements

from Gaia to define our Gaussian priors, which penalize the fit for straying beyond the width, b, away from the mean, a, of the parameter. We use an upper limit for the A_V extinction. See Table 3 of Eastman et al. (2019) for a detailed description of priors in EXOFASTv2. For the choice of priors for [Fe/H] and $T_{\rm eff}$, we use the CHIRON values, since CHIRON has the highest spectral resolution $R = 80,000$ of the spectrographs we used (see Table 4). The resulting EXOFASTv2 values are consistent with the input values from CHIRON. The spectral energy distribution for each star is also taken into account with EXOFASTv2, as shown in Figure 8. The BD parameters are derived with the normalized TESS and LCOGT light curves and non-phase folded RVs into EXOFASTv2 as inputs. The phase folded light curves and RVs are shown in Figure 5 and Figure 6. The non-negligible BD mass is properly accounted for in EXOFASTv2, so no particularly special treatment is needed with regard to deriving the companion masses.

We see bimodality in the posterior distribution for the age (and correlated parameters) of TOI-569, so we present the two most probable solutions resulting from the bimodal posterior distributions with the absolute most probable solution taken as the final adopted value. The most relevant bimodal posterior
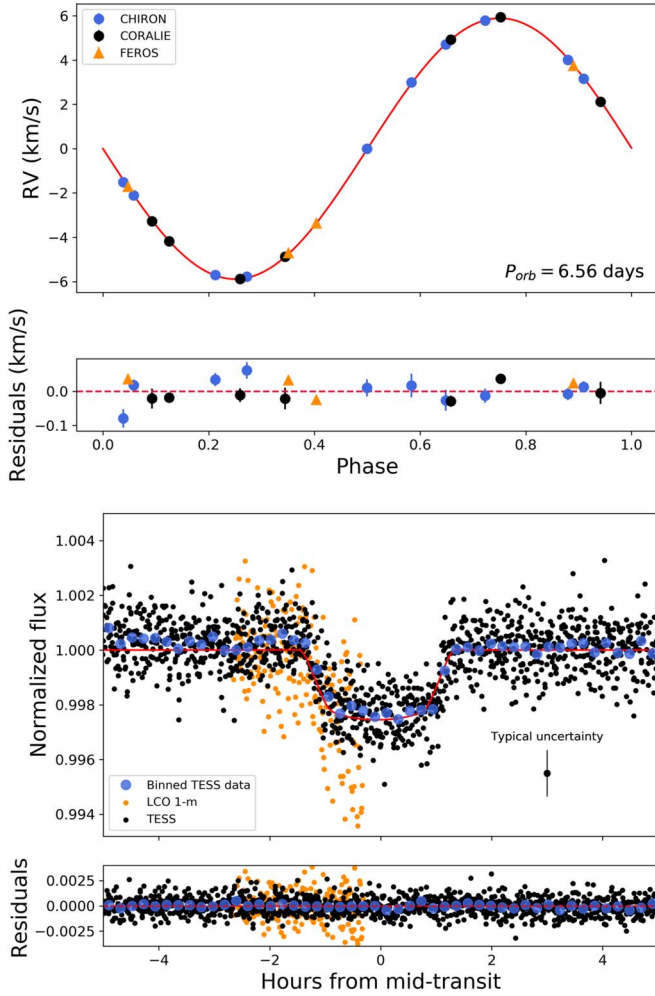
Figure 5. Top: relative radial velocities of TOI-569, with the `EXOFASTv2` orbital solution plotted in red. The orbital eccentricity is consistent with zero ($e < 0.0035$, 1σ upper limit). Bottom: TESS (black) and LCOGT 1 m (orange) light curves with `EXOFASTv2` transit model in red and binned TESS data in blue.

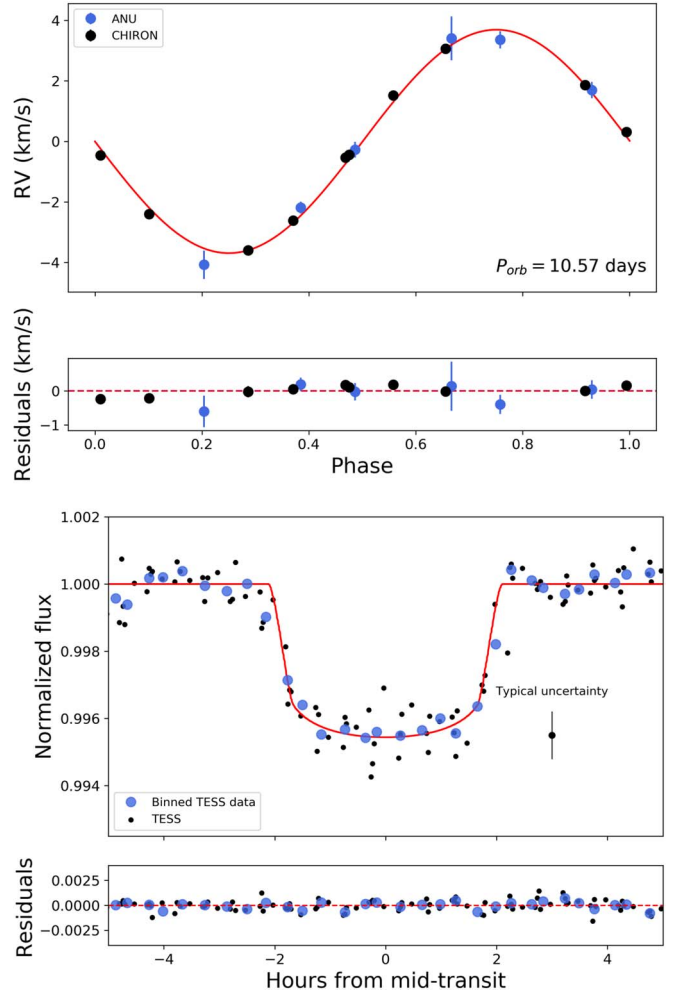**Figure 6.** Top: relative radial velocities of TOI-1406 with `EXOFASTv2` orbital solution plotted in red. The orbital eccentricity is consistent with zero ($e < 0.039$, 1σ upper limit). Bottom: TESS light curve with `EXOFASTv2` transit model in red and binned TESS data in blue.

distributions are shown in Figure 7. The probability of the solution (for age and mass) we report here is 0.73, with the less likely solution having a probability of 0.27.

The resulting stellar SED models from `EXOFASTv2` for TOI-569 and TOI-1406 are shown in Figure 8. These follow the procedures outlined in Stassun & Torres (2016) and Stassun et al. (2017, 2018a).

3.2. Analysis with `pyaneti`

As an independent check on our `EXOFASTv2` analysis, we also carried out an analysis with the `pyaneti`[22] (Barragán et al. 2019) software. Using a Bayesian approach combined with MCMC sampling, we performed a joint analysis of the RV measurements and the TESS light curves, and modeled posterior distributions of the fitted parameters. The RV data were fitted with Keplerian orbits, and for each different instrumental set-up, an offset term for each systemic velocity is included. The non-negligible mass of the brown dwarf is properly taken into account in `pyaneti` (Barragán et al. 2019). The photometric data are modeled with the quadratic limb-darkening model of Mandel & Agol (2002).

---

[22] https://github.com/oscaribv/pyaneti

Table 4
Spectroscopic Values for TOI-569 and TOI-1406 from CHIRON, ANU, CORALIE, and FEROS

TOI-569	CHIRON	CORALIE	FEROS
$T_{\rm eff}$ (K)	5669 ± 106	5481 ± 110	5669 ± 80
$\log g$	4.11 ± 0.18	4.08 ± 0.12	4.21 ± 0.12
[Fe/H] (dex)	$+0.23 \pm 0.05$	$+0.41 \pm 0.09$	$+0.28 \pm 0.05$
FWHM (km s^{-1})	6.65 ± 0.16	10.50 ± 0.50	6.45 ± 0.30
R (resolution)	80,000	60,000	48,000

TOI-1406	ANU	CHIRON	
$T_{\rm eff}$ (K)	6283 ± 110	6347 ± 186	⋯
$\log g$	4.13 ± 0.12	4.09 ± 0.15	⋯
[Fe/H] (dex)	-0.09 ± 0.09	-0.05 ± 0.11	⋯
FWHM (km s^{-1})	15.0 ± 1.0	12.9 ± 0.2	⋯
R (resolution)	23,000	80,000	⋯

Note. We use [Fe/H] and $T_{\rm eff}$ values from CHIRON as inputs to the global model described in Section 3.1.

We use uniform priors and fit for the BD-to-star radius ratio, the orbital period, the mid-transit time, the scaled orbital distance, the eccentricity, the argument of periastron, the
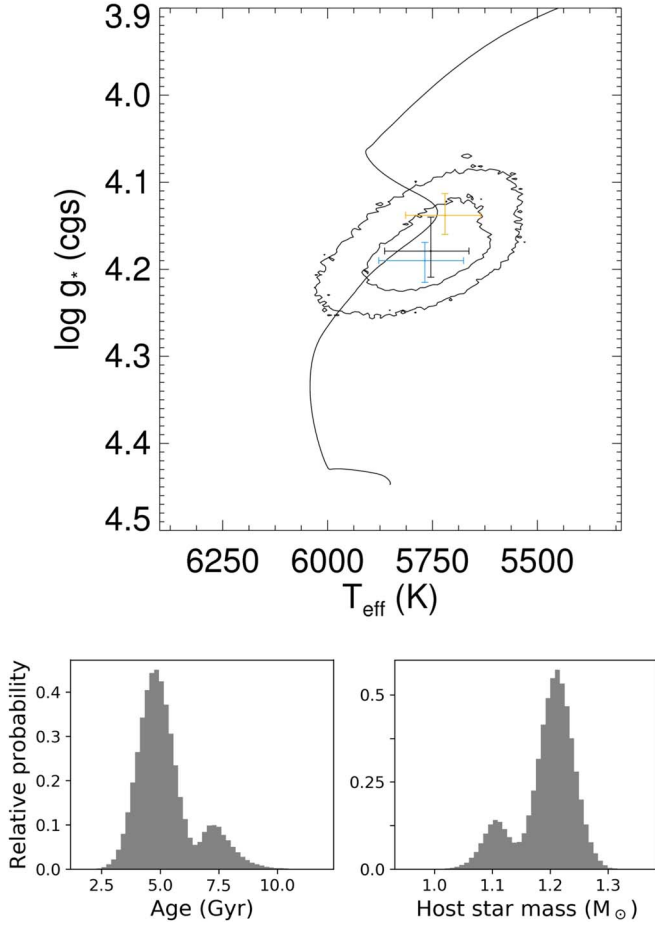
Figure 7. Top: MIST isochrone from `EXOFASTv2` for TOI-569. The best-fitting MIST track is shown by the black line. The median values and 1σ errors from our global fit are shown in the black cross, with the corresponding 3σ contours in black. When splitting this bimodal global solution (black points and contours), the results are the blue and orange crosses. The blue cross shows the higher probability solution for $\log g$ and $T_{\rm eff}$, and the orange cross shows the lower probability solution. Bottom: age and stellar mass posterior distributions from `EXOFASTv2` for TOI-569. We show these to provide a sense of the relative probabilities between the peaks of the bimodal distributions, which is roughly three-to-one in favor of a more massive, younger system (blue cross in top panel). We see no bimodality for the posterior distributions of TOI-1406 in `EXOFASTv2`.
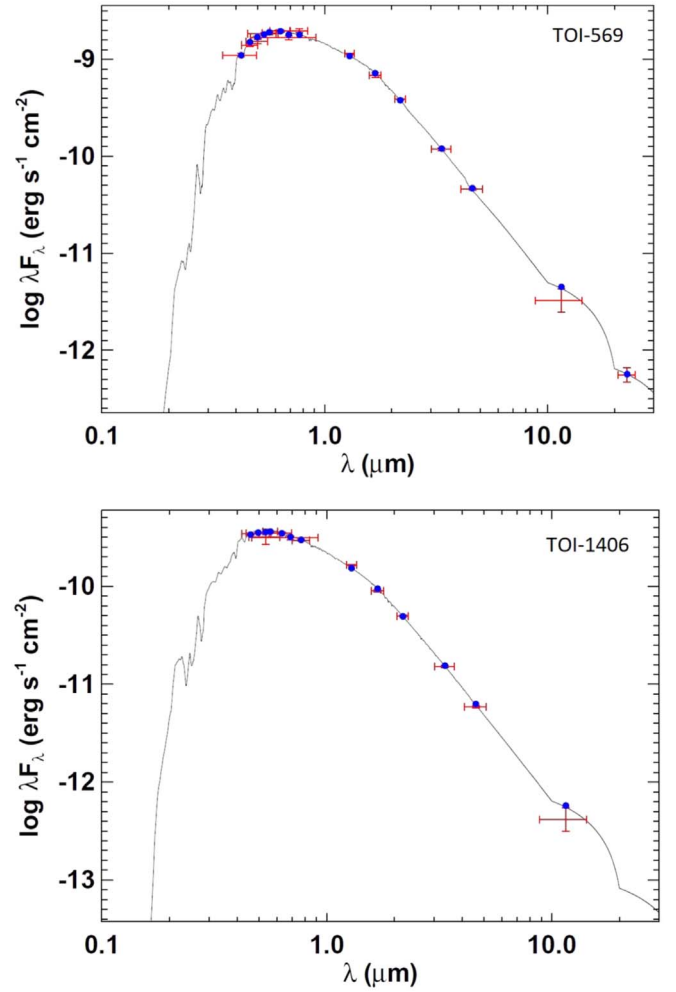

Figure 8. Spectral energy distributions for TOI-569 and TOI-1406. Red symbols represent the observed photometric measurements, where the horizontal bars represent the effective width of the bandpass. Blue symbols are the model fluxes from the best-fit Kurucz atmosphere model (black).

Table 5
Allowed Ranges for Fit Parameters from `pyaneti`

Parameter	TOI-569	TOI-1406
$R_{\rm BD}/R_\star$	[0, 0.1]	[0, 0.1]
$P_{\rm orb}$ (days)	[6.5541, 6.5580]	[10.5721, 10.5762]
$T_0 - 2458400$ (BJD$_{\rm TDB}$)	[96.858, 96.878]	[14.5061, 14.7061]
$a/R_\star$	[1.1, 12]	[1.1, 19]
$e\cos\omega$	[−1, 1]	[−1, 1]
$e\sin\omega$	[−1, 1]	[−1, 1]
Impact parameter b	[0, 1]	[0, 1]
Semi-amplitude K (km s^{-1})	[0, 15]	[0, 15]

impact parameter (b), and the Doppler semi-amplitude variation (K). The allowed ranges for the fit parameters for `pyaneti` are shown in Table 5.

We used 500 independent chains and checked for convergence after every 5000 iterations. After convergence, a posterior distribution of 250,000 independent points for every parameter was computed from the last 500 iterations. We find the eccentricity to be consistent with zero for both BDs. We find a mass and radius of TOI-569b and TOI-1406b to be consistent within 1σ of the values from the `EXOFASTv2` models.

3.3. Rotational Inclination Angle of TOI-569

Astronomers may calculate the angle at which a star is inclined to the line of sight, $I_\star$, in order to learn about the relative alignment between this angle and the orbital inclination angle, i, of a transiting or eclipsing object. Using the spectroscopic $v\sin I_\star$ measurement from CHIRON (the highest resolution spectrograph we used with $R \sim 80{,}000$) and the $P_{\rm rot}$ results from the Lomb–Scargle periodogram analysis, we

calculate the inclination of the rotational axis of TOI-569 to be $I_\star = 65.58^{+17.75}_{-8.55}{}^{\circ}$ (1σ uncertainties). This is traditionally done by taking

$$I_\star = \sin^{-1}\left(\frac{v\sin I_\star}{V_{\rm rot}}\right), \qquad (1)$$

where $v\sin I_\star = 5.33 \pm 0.50$ km s^{-1} and $V_{\rm rot} = 2\pi R_\star/P_{\rm rot} = 5.80 \pm 0.58$ km s^{-1}. However, this traditional technique neglects the fact that the prior on $v\sin I_\star$ and the prior on
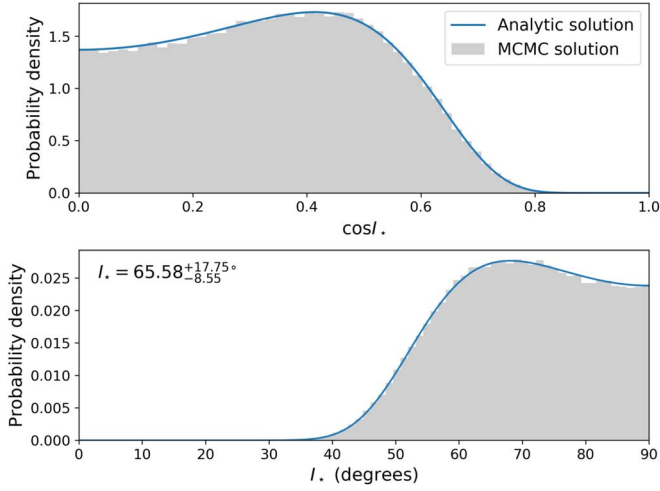
Figure 9. Probability distributions of $\cos I_\star$ and $I_\star$ for TOI-569. The analytic and MCMC solutions follow the procedure outlined by Masuda & Winn (2020).

$V_{\rm rot}$ depend on each other and are therefore covariant. Masuda & Winn (2020) provide guidance on how to properly address this flaw with the traditional technique. We show our results of $I_\star$ for TOI-569 using the formulation described by Masuda & Winn (2020) in Figure 9. We use the MCMC distribution to calculate the 1σ uncertainties as the 16th and 84th percentiles of the distribution, with the mean being the peak of the analytic distribution. We use the peak of the distribution because the distribution is skewed, and so the median would bias $I_\star$ to higher values. This method neglects the effects of differential rotation in the star, which may change the $P_{\rm rot}$ we report here by up to 15%, depending on the latitude of the star spots (Quinn & White 2016).

The orbital inclination of TOI-569b is $i = 85.37^{+0.13\circ}_{-0.11}$. Given the probability distribution of the stellar inclination $I_\star = 65.58^{+17.75\circ}_{-8.55}$ of TOI-569 (see Figure 9), we argue that this system is marginally misaligned and that alignment cannot be ruled out.

When only $v \sin I_\star$ is known, as is the case with TOI-1406, we use the following equation to place an upper limit on $P_{\rm rot}$ (5.3 days), which is much shorter than the orbital period of TOI-1406b (10.6 days), meaning that the system is not synchronized:

$$P_{\rm rot} \leqslant \frac{2\pi R_\star}{v \sin I_\star}. \tag{2}$$

3.4. Tidal Circularization Timescales

Over time, tidal interactions between a host star and any companions affect their orbits. Generally, the orbits of the companions and their host stars first begin to circularize according to what is known as the *circularization timescale*. Next, the orbital period of the companion synchronizes with their host star's rotation (the synchronization timescale). Finally, the system experiences a spin–orbit co-alignment (Mazeh 2008). These timescales are influenced by the mass, radius, separation, and tidal quality factor Q of both the host star and companion of a system. Here, we restrict our discussion to the circularization timescales for different values

of the tidal quality factors, $Q_\star$ and $Q_{\rm BD}$, that may be most appropriate for the TOI-569 and TOI-1406 systems.

Following the formalism from Jackson et al. (2008), the equations for the orbital circularization timescale for a close-in companion are

$$\frac{1}{\tau_{\rm circ,\star}} = \frac{171}{16} \sqrt{\frac{G}{M_\star}} \frac{R_\star^5 M_{\rm BD}}{Q_\star} a^{-\frac{13}{2}} \tag{3}$$

$$\frac{1}{\tau_{\rm circ,BD}} = \frac{63}{4} \frac{\sqrt{GM_\star^3} R_{\rm BD}^5}{Q_{\rm BD} M_{\rm BD}} a^{-\frac{13}{2}} \tag{4}$$

$$\frac{1}{\tau_{\rm e}} = \frac{1}{\tau_{\rm circ,\star}} + \frac{1}{\tau_{\rm circ,BD}}, \tag{5}$$

where $\tau_{\rm e}$ is the circularization timescale, a is the semimajor axis, $M_\star$ is the stellar mass, $R_\star$ is the stellar radius, $M_{\rm BD}$ is the BD mass, $R_{\rm BD}$ is the BD radius, $Q_\star$ is the tidal quality factor for the star, and $Q_{\rm BD}$ is the tidal quality factor for the BD. Equation (5) is a prediction on how long it takes for the orbital eccentricity of an object to decrease by an exponential factor (the relationship $\tau_{\rm e} \propto dt \propto -de/e$), based on the tides raised on the star and BD.

Use of this equation comes with a number of assumptions that we reiterate here from Jackson et al. (2008): (1) the BD is in a short orbital period (10 days or less), (2) the orbital eccentricity e is small (though for companions in the planetary mass range, higher-order terms may be important to account for higher e in the past), (3) the BD's orbital period $P_{\rm orb}$ is smaller than the host star's rotation period $P_{\rm rot}$, and (4) $Q_\star$ is independent of the tidal forcing frequency. Admittedly, Equation (5) and these assumptions cater to hot Jupiters and not the type of more massive BDs in this study.

With these considerations in mind, we calculate $\tau_{\rm e}$ for TOI-569b and TOI-1406b for a range of $Q_\star$ and $Q_{\rm BD}$ for each system in Table 6. The choice to adopt a $Q_{\rm BD}$ as low as $10^{4.5}$ comes from Beatty et al. (2018), who directly constrain $Q_{\rm BD}$ for CWW 89Ab, a $M_{\rm BD} = 39 M_{\rm J}$ BD. The choice to adopt a $Q_\star$ as low as 10^5 comes from studies of circularization of binary stars (Meibom & Mathieu 2005; Milliman et al. 2014). For the bimodal posterior distributions of TOI-569, we only use the most probable $M_\star$, $R_\star$, $M_{\rm BD}$, $R_{\rm BD}$, and a.

We highlight the tidal theory here to show that for these BDs, it is difficult to pin down the timescale over which tidal interactions influence their orbits. Though both BDs have circular orbits, we may only conclude that TOI-1406b likely underwent a low-eccentricity migration, unless tidal dissipation was extremely efficient. The circularization timescales for TOI-569 may be short enough such that tidal interactions alone would have circularized the orbit of the BD over the system's age, thus making it difficult to tell whether or not the BD formed in a circular orbit.

4. Discussion

Including the 2 new BDs in this work, the total number of known BDs that transit a star is 23 (Table 7). With the discovery of TOI-569b and TOI-1406b, the total number of new transiting BDs discovered or observed by the TESS mission is now 4 (Jackman et al. 2019; Subjak et al. 2020; this work). We expect at least as many more to be discovered as TESS continues its observations over the remainder of its

Table 6
Circularization Timescales for Different Values of $Q_\star$ and Q_{BD}, with Stellar Rotational Period and BD Orbital Period also Shown

Object Name and Age	$Q_\star$	Q_{BD}	τ_e (Gyr)
TOI-569	10^7	10^6	$8.0^{+0.8}_{-1.2}$
$4.70^{+1.30}_{-1.30}$ Gyr	10^7	$10^{4.5}$	$7.5^{+0.7}_{-1.1}$
	10^6	$10^{4.5}$	$0.80^{+0.08}_{-0.12}$
	10^5	$10^{4.5}$	$0.08^{+0.01}_{-0.01}$
TOI-1406	10^7	10^6	$127^{+26.2}_{-24.1}$
$3.20^{+2.20}_{-1.60}$ Gyr	10^7	$10^{4.5}$	$91.5^{+18.4}_{-17.0}$
	10^6	$10^{4.5}$	$12.4^{+2.5}_{-2.3}$
	10^5	$10^{4.5}$	$1.3^{+0.3}_{-0.2}$

	P_{rot} (days)	P_{orb} (days)	$v \sin I_\star$ (km s^{-1})
TOI-569	12.9	6.6	5.3 ± 0.5

	P_{rot} (days)	P_{orb} (days)	FWHM (km s^{-1})
TOI-1406	$\leqslant 5.3$	10.6	12.9 ± 0.2

Note. We quote the rotation period measured from the periodogram of the TESS light curve for TOI-569. An upper limit on the rotation period of TOI-1406 is calculated (Equation (2)) using $R_\star$ from EXOFASTv2 and FWHM as an approximation for $v \sin I_\star$. Since we do not directly have the inclination of the star's rotation axis for TOI-1406, the rotation period listed for this star is an upper limit. The $v \sin I_\star$ and FWHM values are from CHIRON. These show 1σ uncertainties.

primary mission. At present, we do not have enough transiting BDs to perform a statistical study of the population and draw conclusions about the fundamental origins of BDs, and how the mass, radius, and orbital properties of a BD reflects its formation and evolution.

Mass, radius, age, and orbital properties are some of the key aspects that make up a complete understanding of the formation of transiting BDs. Traditionally, astronomers have defined BDs based on their ability to fuse deuterium and their inability to fuse hydrogen. Implicit in this definition is the assumption that BD formation is solely a function of mass. While it may be the case that mass is one of the more important factors in determining whether or not an object is a giant planet, BD, or low-mass star, there is a wealth of evolutionary information to be found in other basic properties.

As we have explored here, the radius, age, and orbital eccentricity give us greater leverage toward understanding transiting BDs. We may combine orbital eccentricity and age with our knowledge of tidal timescales to examine the orbital history of a transiting BD. When the radius and age are used with the mass, we acquire a foothold into the mass–radius diagram for transiting BDs, where we may directly test the accuracy of substellar evolutionary models that seek to explain the underlying physics behind transiting BD formation. In this section, we will look at the population of transiting BDs and discuss how TOI-569b and TOI-1406b fit into this picture.

4.1. Transiting Brown Dwarf Host Star Distribution

The mass distribution for the current population of transiting BDs is shown in Figure 10, with the effective temperature of the host star indicated by the colors of the points. From all published studies of transiting BDs to date, there is no obvious preference for a particular type of star to host transiting BDs. Interestingly, we see that six transiting BDs (roughly 20% of
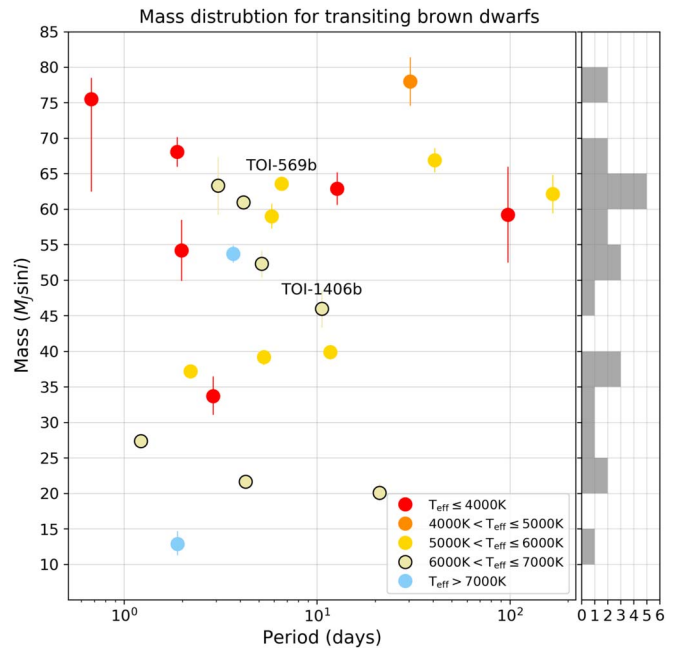

Figure 10. Mass–period distribution of transiting BDs. The colors indicate the effective temperature of the host star of each BD.

the transiting BD population, see Table 7) are hosted by an M dwarf star. This is in contrast to hot Jupiters, where only a small percentage of the hot Jupiter population is found transiting M dwarf stars (e.g., Kepler-45b Johnson et al. 2012, HATS-6b Hartman et al. 2015, WASP-80b Triaud et al. 2015, NGTS-1b Bayliss et al. 2018). By placing the transiting BD population in the context of eclipsing low-mass stars and hot Jupiters, we may also explore the idea that the scarcity of transiting BDs stems from them, spanning the space between the tail ends of the distributions for companions that form like giant planets versus companions that form like low-mass stars. However, more transiting BD discoveries are needed for such studies to yield meaningful results.

4.2. Substellar Isochrones and the Mass–Radius Diagram

Here we will discuss how we use transiting BDs with well-determined masses, radii, and ages to test the substellar isochrones from Baraffe et al. (2003; for irradiated BDs) and Saumon & Marley (2008; for non-irradiated BDs). The Baraffe et al. (2003) models use the same input physics that Chabrier & Baraffe (1997) used for main-sequence stars. These are scaled appropriately in Baraffe et al. (2003) for low-mass stars and substellar objects down to $\lesssim 1 M_J$. The way we test these models is by having independent measurements of a transiting BD's age, which comes from the age of its host star (assuming the BD is the same age as its host star). We prioritize the use of stellar ages obtained through studies of clusters, asteroseismology, and gyrochronology, but with Gaia DR2, we are able to reliably determine stellar properties to derive accurate ages with stellar isochrone models such as MIST. This increases the number of transiting BDs for which we have reliable and independently determined ages for comparison to substellar isochrones. This is important because we only know the companion as well as we know the host star, and with Gaia DR2, we can now examine the host star with greater precision than ever before.

Table 7
List of Published Transiting Brown Dwarfs as of 2019 September

Name	P (days)	M_{BD}/M_J	R_{BD}/R_J	e	$M_\star/M_\odot$	$R_\star/R_\odot$	T_{eff} (K)	[Fe/H]	References
TOI-569b	6.556	64.1 ± 1.9	0.75 ± 0.02	<0.0035	1.21 ± 0.05	1.47 ± 0.03	5768 ± 110	+0.29 ± 0.09	this work
TOI-1406b	10.574	46.0 ± 2.7	0.86 ± 0.03	<0.039	1.18 ± 0.09	1.35 ± 0.03	6290 ± 100	−0.08 ± 0.09	this work
HATS-70b	1.888	12.9 ± 1.8	1.38 ± 0.08	<0.18	1.78 ± 0.12	1.88 ± 0.07	7930 ± 820	+0.04 ± 0.11	1
KELT-1b	1.218	27.4 ± 0.9	1.12 ± 0.04	0.01 ± 0.01	1.34 ± 0.06	1.47 ± 0.05	6516 ± 49	+0.05 ± 0.08	2
NLTT 41135b	2.889	33.7 ± 2.8	1.13 ± 0.27	<0.02	0.19 ± 0.03	0.21 ± 0.02	3230 ± 130	−0.25 ± 0.25	3
LHS 6343c	12.713	62.9 ± 2.3	0.83 ± 0.02	0.056 ± 0.032	0.37 ± 0.01	0.38 ± 0.01	⋯	+0.02 ± 0.19	4
LP 261-75b	1.882	68.1 ± 2.1	0.90 ± 0.02	<0.007	0.30 ± 0.02	0.31 ± 0.01	3100 ± 50	⋯	5
WASP-30b	4.157	61.0 ± 0.9	0.89 ± 0.02	0 (adopted)	1.17 ± 0.03	1.30 ± 0.02	6201 ± 97	−0.08 ± 0.10	6
WASP-128b	2.209	37.2 ± 0.9	0.94 ± 0.02	<0.007	1.16 ± 0.04	1.15 ± 0.02	5950 ± 50	+0.01 ± 0.12	7
CoRoT-3b	4.257	21.7 ± 1.0	1.01 ± 0.07	0 (adopted)	1.37 ± 0.09	1.56 ± 0.09	6740 ± 140	−0.02 ± 0.06	8
CoRoT-15b	3.060	63.3 ± 4.1	1.12 ± 0.30	0 (adopted)	1.32 ± 0.12	1.46 ± 0.31	6350 ± 200	+0.10 ± 0.20	9
CoRoT-33b	5.819	59.0 ± 1.8	1.10 ± 0.53	0.070 ± 0.002	0.86 ± 0.04	0.94 ± 0.14	5225 ± 80	+0.44 ± 0.10	10
Kepler-39b	21.087	20.1 ± 1.3	1.24 ± 0.10	0.112 ± 0.057	1.29 ± 0.07	1.40 ± 0.10	6350 ± 100	+0.10 ± 0.14	11
KOI-189b	30.360	78.0 ± 3.4	1.00 ± 0.02	0.275 ± 0.004	0.76 ± 0.05	0.73 ± 0.02	4952 ± 40	−0.07 ± 0.12	12
KOI-205b	11.720	39.9 ± 1.0	0.81 ± 0.02	<0.031	0.92 ± 0.03	0.84 ± 0.02	5237 ± 60	+0.14 ± 0.12	13
KOI-415b	166.788	62.1 ± 2.7	0.79 ± 0.12	0.689 ± 0.001	0.94 ± 0.06	1.15 ± 0.15	5810 ± 80	−0.24 ± 0.11	14
EPIC 201702477b	40.737	66.9 ± 1.7	0.76 ± 0.07	0.228 ± 0.003	0.87 ± 0.03	0.90 ± 0.06	5517 ± 70	−0.16 ± 0.05	15
EPIC 212036875b	5.170	52.3 ± 1.9	0.87 ± 0.02	0.132 ± 0.004	1.29 ± 0.07	1.50 ± 0.03	6238 ± 60	+0.01 ± 0.10	18, 21
AD 3116b	1.983	54.2 ± 4.3	1.02 ± 0.28	0.146 ± 0.024	0.28 ± 0.02	0.29 ± 0.08	3200 ± 200	+0.16 ± 0.10	17
CWW 89Ab	5.293	39.2 ± 1.1	0.94 ± 0.02	0.189 ± 0.002	1.10 ± 0.05	1.03 ± 0.02	5755 ± 49	+0.20 ± 0.09	16, 18
RIK 72b	97.760	59.2 ± 6.8	3.10 ± 0.31	0.146 ± 0.012	0.44 ± 0.04	0.96 ± 0.10	3349 ± 142	⋯	19
TOI-503b	3.677	53.7 ± 1.2	$1.34^{+0.26}_{-0.15}$	0 (adopted)	1.80 ± 0.06	1.70 ± 0.05	7650 ± 160	+0.61 ± 0.07	22
NGTS-7Ab	0.676	$75.5^{+3.0}_{-13.7}$	$1.38^{+0.13}_{-0.14}$	0 (adopted)	0.48 ± 0.13	0.61 ± 0.06	3359 ± 106	⋯	23
2M0535-05a[g]	9.779	56.7 ± 4.8	6.50 ± 0.33	0.323 ± 0.006	⋯	⋯	⋯	⋯	20
2M0535-05b[f]	9.779	35.6 ± 2.8	5.00 ± 0.25	0.323 ± 0.006	⋯	⋯	⋯	⋯	20

References. (1) Zhou et al. (2019), (2) Siverd et al. (2012), (3) Irwin et al. (2010), (4) Johnson et al. (2011), (5) Irwin et al. (2018), (6) Anderson et al. (2011), (7) Hodžić et al. (2018), (8) Deleuil et al. (2008), (9) Bouchy et al. (2011), (10) Csizmadia et al. (2015), (11) Bonomo et al. (2015), (12) Díaz et al. (2014), (13) Díaz et al. (2013), (14) Moutou et al. (2013), (15) Bayliss et al. (2017), (16) Nowak et al. (2017), (17) Gillen et al. (2017), (18) Carmichael et al. (2019), (19) David et al. (2019), (20) Stassun et al. (2006), (21) Persson et al. (2019), (22) Subjak et al. (2020), (23) Jackman et al. (2019).

The mass–radius diagram for transiting BDs is shown in Figure 11. All of the BDs on this diagram are necessarily transiting because it is through the transit method that we can measure the radius. However, even though a transit provides some measure of the radius, the measurement is not always very precise (i.e., as precise as the measurement of the stellar radius). This is important because the radius of a BD changes drastically with its age (see Baraffe et al. 2003). Substellar isochrones are challenging to test at ages beyond a few Gyr because the rate at which BD radii contract significantly decelerates, resulting in transiting BD radii approaching an asymptotic limit for the oldest systems (see the differences between the 3 and 10 Gyr substellar isochrones in Figure 11).

Taking a more critical look at Figure 11, we notice some interesting features. Among the most noticeable are the large (>10%) uncertainties on the radii of no fewer than six transiting BDs (AD 3116b, CoRoT-15b, CoRoT-33b, NGTS-7b, NLTT 41135b, and TOI-503b). These are the least informative data points in the substellar mass–radius diagram, especially for objects younger than 1 Gyr, as the radius of a transiting BD changes rapidly at ages less than 1 Gyr. Notice also how the substellar isochrone models are mostly horizontal from roughly 20 to 70 M_J. This means that testing the age of the isochrones is less sensitive to the precision on the mass than the precision on the radius of a transiting BD.

Interestingly, the oldest substellar isochrones are traced fairly well by a handful of transiting BDs. This suggests that the oldest substellar isochrones accurately predict the radii of transiting BDs that approach this asymptotic limit. Future

works to improve on the Baraffe et al. (2003; COND03) and Saumon & Marley (2008; SM08) models must consider the effects of metallicity for transiting BDs, as this may be key to more finely distinguishing the older substellar isochrones from each other, especially in the asymptotic radius regime of 20 to 70 M_J. The COND03 models do not explore a variety of different metallicity values, as the SM08 models do, but the SM08 models do not consider the effects of irradiation like the COND03 models. Additionally, improvements may be made to BDs less massive than 20 M_J, as the input physical prescription from Baraffe et al. (2003) and Chabrier & Baraffe (1997) may not describe these BDs as well as they do more massive objects.

4.2.1. TOI-569b and TOI-1406b in the Mass–Radius Diagram

TOI-569b and TOI-1406b provide us with the opportunity to test substellar isochrones older than 2.5 Gyr for the first time because we have accurate masses, radii, and ages traceable to stellar isochrones for their host stars. In this sense, we are using well-tested stellar isochrones to examine relatively untested substellar isochrones. The parameters for the host stars and BDs for these two systems are shown in Tables 8 and 9.

Both the COND03 and the SM08 models seem to slightly overestimate the age of TOI-569b to be ∼10 Gyr compared to the age of the host star modeled from the MIST isochrones (4.70 ± 1.30 Gyr). However, we note that the lower probability bimodal solution for TOI-569b favors a system age of 7.50 ± 1.80 Gyr, which is in better agreement with the

Table 8
MIST Median Values and 68% Confidence Interval for TOI-1406, Created Using EXOFASTv2 Commit Number 65aa674

Parameter	Units	Priors	Values
Stellar Parameters:			
M_*	Mass ($M_\odot$)	⋯	$1.18^{+0.08}_{-0.09}$
R_*	Radius ($R_\odot$)	⋯	$1.35^{+0.03}_{-0.03}$
L_*	Luminosity ($L_\odot$)	⋯	2.56 ± 0.15
ρ_*	Density (cgs)	⋯	$0.68^{+0.07}_{-0.07}$
$\log g$	Surface gravity (cgs)	⋯	$4.252^{+0.037}_{-0.041}$
$T_{\rm eff}$	Effective temperature (K)	$\mathcal{G}[6347, 186]$	6290 ± 100
[Fe/H]	Metallicity (dex)	$\mathcal{G}[-0.05, 0.11]$	-0.08 ± 0.09
Age	Age (Gyr)	⋯	$3.20^{+2.20}_{-1.60}$
EEP	Equal evolutionary point	⋯	377^{+40}_{-36}
A_V	V-band extinction (mag)	$\mathcal{U}[0, 0.08804]$	$0.043^{+0.030}_{-0.029}$
$\sigma_{\rm SED}$	SED photometry error scaling	⋯	$3.04^{+1.2}_{-0.73}$
ϖ	Parallax (mas)	$\mathcal{G}[2.3855, 0.0291]$	2.386 ± 0.029
d	Distance (pc)	⋯	$419.1^{+5.2}_{-5.0}$
$v \sin I_\star$	Projected equatorial velocity (km s^{-1})	Not modeled	12.91 ± 0.24
Brown Dwarf Parameters:			
P	Period (days)	⋯	$10.57398^{+0.00060}_{-0.00059}$
M_P	Mass ($M_{\rm J}$)	⋯	$46.0^{+2.6}_{-2.7}$
R_P	Radius ($R_{\rm J}$)	⋯	0.86 ± 0.03
T_C	Time of conjunction (BJD$_{\rm TDB}$)	⋯	$2458414.6065^{+0.0018}_{-0.0019}$
a	Semimajor axis (au)	⋯	$0.1010^{+0.0022}_{-0.0026}$
i	Orbital inclination (°)	⋯	$87.70^{+0.19}_{-0.20}$
e	Eccentricity	⋯	$0.026^{+0.013}_{-0.010}$
$e \cos \omega_*$		⋯	$-0.0160^{+0.0079}_{-0.0071}$
$e \sin \omega_*$		⋯	$0.017^{+0.017}_{-0.015}$
$T_{\rm eq}$	Equilibrium temperature (K)	⋯	1108^{+18}_{-17}
K	RV semi-amplitude (m s^{-1})	⋯	3720^{+120}_{-130}
$\log K$	Log of RV semi-amplitude	⋯	$3.570^{+0.014}_{-0.015}$
R_P/R_*	Radius of planet in stellar radii	⋯	0.0654 ± 0.0011
a/R_*	Semimajor axis in stellar radii	⋯	$16.11^{+0.56}_{-0.58}$
δ	Transit depth (fraction)	⋯	0.00428 ± 0.00014
τ	Ingress/egress transit duration (days)	⋯	$0.0180^{+0.0016}_{-0.0014}$
b	Transit impact parameter	⋯	$0.648^{+0.033}_{-0.036}$
ρ_P	Density (cgs)	⋯	$90^{+11}_{-10.}$
$\log g_P$	Surface gravity	⋯	$5.190^{+0.040}_{-0.042}$
$M_P \sin i$	Minimum mass ($M_{\rm J}$)	⋯	$45.9^{+2.6}_{-2.7}$
M_P/M_*	Mass ratio	⋯	$0.0372^{+0.0016}_{-0.0015}$

Wavelength Parameters:		TESS band	
u_1	Linear limb-darkening coeff	0.224 ± 0.050	
u_2	Quadratic limb-darkening coeff	0.299 ± 0.050	
RV Parameters:		ANU	CHIRON
$\gamma_{\rm rel}$	Relative RV offset (m s^{-1})	-15490^{+200}_{-240}	-15461^{+70}_{-68}
σ_J	RV jitter (m s^{-1})	380^{+400}_{-260}	182^{+85}_{-56}
σ_J^2	RV jitter variance	$150000^{+460000}_{-130000}$	33000^{+38000}_{-17000}
Transit Parameters:		TESS	
σ^2	Added variance	$-0.000000154^{+0.000000011}_{-0.000000010}$	
F_0	Baseline flux	0.999996 ± 0.000013	

Note. Here, $\mathcal{U}[a, b]$ is the uniform prior bounded between a and b, and $\mathcal{G}[a, b]$ is a Gaussian prior of mean a and width b. We show $v \sin I_\star$ (taken to be the FWHM measured from CHIRON) only for convenient reference; EXOFASTv2 does not model FWHM for spectral line broadening.

COND03 and SM08 models. The log g of TOI-569 also favors an older system.

Something else worth note is that for a fixed BD mass and age, the radius increases with increasing metallicity (Burrows et al. 2011), and yet, TOI-569b has one of the smallest radii of all known transiting BDs with [Fe/H] = +0.29 dex (assuming it matches the host star). When referencing Burrows et al. (2011),

Figure 1, we expect a change in the BD's metallicity ([Fe/H]) from +0.0 to +0.5 dex to result as a roughly 0.05–0.1 $R_{\rm J}$ increase in the radius of the BD. There is also an increase of about 0.05 $R_{\rm J}$ when transitioning from clear to cloudy atmospheric models for the BD. This is roughly a factor of two larger than our uncertainties on the radius TOI-569b ($R_{\rm BD} = 0.75 \pm 0.02$ $R_{\rm J}$). For TOI-1406, we find that both the COND03 and SM08

Table 9
MIST Median Values and 68% Confidence Interval for TOI-569, Created Using `EXOFASTv2` Commit Number 65aa674

Parameter	Units	Priors	Most-likely Values	Less-likely Values
Stellar Parameters:			**Prob. = 0.73**	Prob. = 0.27
M_*	Mass ($M_\odot$)	...	**1.21 ± 0.05**	$1.10^{+0.03}_{-0.05}$
R_*	Radius ($R_\odot$)	...	**1.48 ± 0.03**	1.48 ± 0.03
L_*	Luminosity ($L_\odot$)	...	**$2.15^{+0.15}_{-0.12}$**	2.09 ± 0.1
ρ_*	Density (cgs)	...	**0.54 ± 0.04**	0.48 ± 0.03
$\log g$	Surface gravity (cgs)	...	**4.19 ± 0.03**	4.14 ± 0.02
$T_{\rm eff}$	Effective temperature (K)	$\mathcal{G}[5699, 106]$	**5768^{+110}_{-92}**	5720^{+94}_{-85}
[Fe/H]	Metallicity (dex)	$\mathcal{G}[+0.23, 0.10]$	**$+0.29^{+0.09}_{-0.08}$**	+0.23 ± 0.09
Age	Age (Gyr)	...	**4.70 ± 1.3**	$7.50^{+1.80}_{-1.20}$
A_V	V-band extinction (mag)	$\mathcal{U}[0, 1.1749]$	**$0.067^{+0.083}_{-0.049}$**	$0.052^{+0.074}_{-0.038}$
$\sigma_{\rm SED}$	SED photometry error scaling	...	**$2.99^{+1.10}_{-0.71}$**	$3.08^{+1.40}_{-0.78}$
ϖ	Parallax (mas)	$\mathcal{G}[6.3723, 0.0306]$	**6.374 ± 0.031**	$6.374^{+0.031}_{-0.030}$
d	Distance (pc)	...	**156.88 ± 0.75**	156.83 ± 0.75
$v \sin I_\star$	Projected equatorial velocity (km s^{-1})	Not modeled	**5.30 ± 0.50**	5.30 ± 0.50
Brown Dwarf Parameters:				
P	Period (days)	...	**$6.55604^{+0.00016}_{-0.00015}$**	$6.55603^{+0.00016}_{-0.00015}$
M_P	Mass (M_J)	...	**$64.1^{+1.9}_{-1.4}$**	$59.6^{+1.1}_{-1.7}$
R_P	Radius (R_J)	...	**0.75 ± 0.02**	0.76 ± 0.02
T_C	Time of conjunction (BJD$_{\rm TDB}$)	...	**$2458523.09192^{+0.00070}_{-0.00069}$**	2458523.09199 ± 0.00070
a	Semimajor axis (au)	...	**0.07428 ± 0.00059**	$0.07207^{+0.00047}_{-0.00069}$
i	Orbital inclination (°)	...	**$85.37^{+0.13}_{-0.11}$**	$85.15^{+0.13}_{-0.12}$
e	Eccentricity	...	**$0.0017^{+0.0018}_{-0.0012}$**	$0.0017^{+0.0018}_{-0.0012}$
$e \cos \omega_*$		...	**$0.0002^{+0.0015}_{-0.0011}$**	$0.0002^{+0.0015}_{-0.0011}$
$e \sin \omega_*$		...	**$0.0005^{+0.0022}_{-0.0012}$**	$0.0005^{+0.0022}_{-0.0012}$
$T_{\rm eq}$	Equilibrium temperature (K)	...	**1227^{+13}_{-12}**	1237^{+12}_{-13}
K	RV semi-amplitude (m s^{-1})	...	**5884 ± 17**	5884^{+18}_{-17}
$\log K$	Log of RV semi-amplitude	...	**3.7697 ± 0.0013**	3.7697 ± 0.0013
R_P/R_*	Radius of planet in stellar radii	...	**$0.05217^{+0.00094}_{-0.00091}$**	$0.05258^{+0.0010}_{-0.00096}$
a/R_*	Semimajor axis in stellar radii	...	**$10.81^{+0.22}_{-0.21}$**	$10.44^{+0.21}_{-0.20}$
δ	Transit depth (fraction)	...	**$0.002721^{+0.00010}_{-0.000096}$**	$0.002765^{+0.00011}_{-0.000100}$
τ	Ingress/egress transit duration (days)	...	**$0.0214^{+0.0015}_{-0.0013}$**	$0.0230^{+0.0014}_{-0.0013}$
b	Transit impact parameter	...	**$0.8739^{+0.0082}_{-0.0084}$**	$0.8820^{+0.0068}_{-0.0075}$
ρ_P	Density (cgs)	...	**187^{+17}_{-16}**	169^{+16}_{-15}
$\log g_P$	Surface gravity	...	**$5.444^{+0.029}_{-0.031}$**	$5.412^{+0.027}_{-0.026}$
$M_P \sin i$	Minimum mass (M_J)	...	**63.6 ± 1.0**	$59.9^{+0.8}_{-0.9}$
M_P/M_*	Mass ratio	...	**$0.05043^{+0.00097}_{-0.00050}$**	$0.05195^{+0.00045}_{-0.00039}$

Wavelength Parameters:		*I*-band	TESS band	
u_1	Linear limb-darkening coeff	0.292 ± 0.050	0.335 ± 0.049	
u_2	Quadratic limb-darkening coeff	0.260 ± 0.050	0.269 ± 0.049	
RV Parameters:		CHIRON	CORALIE	FEROS
$\gamma_{\rm rel}$	Relative RV offset (m s^{-1})	71964^{+14}_{-16}	73413^{+17}_{-18}	73402^{+63}_{-55}
σ_J	RV jitter (m s^{-1})	37^{+23}_{-17}	37^{+27}_{-16}	70^{+210}_{-70}
σ_J^2	RV jitter variance	1420^{+2300}_{-1000}	1390^{+2800}_{-920}	5000^{+76000}_{-7100}
Transit Parameters:		LCOGT UT 2019-04-15 (*I*-band)	TESS	
σ^2	Added variance	$0.00000202^{+0.00000030}_{-0.00000026}$	$0.0000001792^{+0.0000000063}_{-0.0000000062}$	
F_0	Baseline flux	0.99981 ± 0.00013	1.0000143 ± 0.0000053	

Note. The most likely values (probability of 0.73) and the ones we report for this system are shown in boldface. Here, $\mathcal{U}[a, b]$ is the uniform prior bounded between a and b, and $\mathcal{G}[a, b]$ is a Gaussian prior of mean a and width b. We show $v \sin I_\star$ (measured from CHIRON) only for convenient reference; `EXOFASTv2` does not model $v \sin I_\star$.

models are fairly efficient at predicting the age of the system ($3.20^{+2.20}_{-1.60}$ Gyr).

4.3. Summary

TOI-569b and TOI-1406b are two newly discovered BDs that transit their host stars in nearly circular orbits. TOI-569 appears to be a slightly evolved G dwarf star with strong photometric modulation interpreted as evolving star spots on the surface of the star. We use the TESS and WASP light curves to extract an estimate for the rotation period of this star to be 13 days and determine that the star's rotational axis is marginally misaligned with the orbital inclination of TOI-569b. In contrast, TOI-1406 is an F star on the main sequence, and with no noticeable photometric modulation over the sectors, the star was observed by TESS. By comparing the ages of each
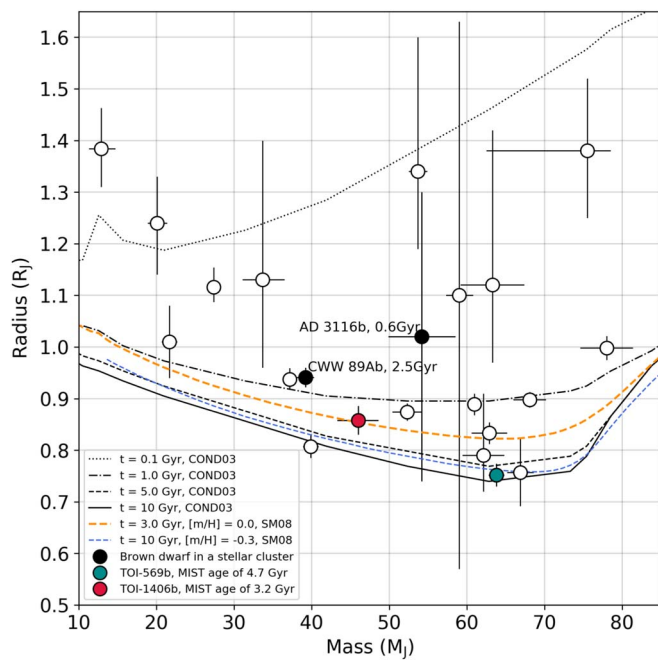
Figure 11. Mass–radius diagram of transiting BDs featuring the COND03 and SM08 models. TOI-569b and TOI-1406 are shown as a cyan point and a red point, respectively. Only three BDs that transit main-sequence stars have ages constrained by stellar clusters or associations (AD 3116b in Preasepe, CWW 89Ab in Ruprecht 147, and RIK 72b in Upper Scorpius). Note RIK 72b is 5–10 Myr old (David et al. 2019) and is not shown because its radius is 3.1 R_J. Also not shown are the eclipsing BDs in the BD binary system, 2M0535-05, located in the Orion Nebula Cluster with an age of 1–2 Myr. Though TOI-569b and TOI-1406b are not in star clusters, we still have relatively precise ages for both from stellar isochrones of their host stars, and in a location on the mass–radius diagram where an age range of 5–10 Gyr results in little change in the models.

system to a range of plausible circularization timescales, we find that we are not able to convincingly determine the orbital history of TOI-569 and that we can at least rule out significant high-eccentricity orbital evolution followed by tidal circularization for TOI-1406.

We demonstrate here how stellar isochrones can be used to test substellar isochrones. This is done by leveraging Gaia DR2 for precise stellar parameters, which translate into better estimates of masses, radii, and ages, of transiting BD.

Ultimately, we find TOI-569b and TOI-1406b to be special in that they contribute new measurements to the still sparsely populated mass–radius diagram for transiting BDs. In addition to providing some of the first examples of a test of the COND03 and SM08 models against stellar isochrones, these systems also offer themselves as new data to examine circularization models. As we build the population of transiting BDs, we will refine the predictive power of substellar isochrones and potentially turn them into tools that are useful for estimating the ages of transiting BDs.

ORCID iDs

Theron W. Carmichael https://orcid.org/0000-0001-6416-1274
Samuel N. Quinn https://orcid.org/0000-0002-8964-8377
Chelsea Huang https://orcid.org/0000-0003-0918-7484
George Zhou https://orcid.org/0000-0002-4891-3517
Karen A. Collins https://orcid.org/0000-0001-6588-9574
Carl Ziegler https://orcid.org/0000-0002-0619-7639
Kevin I. Collins https://orcid.org/0000-0003-2781-3207
Joseph E. Rodriguez https://orcid.org/0000-0001-8812-0565
Avi Shporer https://orcid.org/0000-0002-1836-3120
Rafael Brahm https://orcid.org/0000-0002-9158-7315
Andrew W. Mann https://orcid.org/0000-0003-3654-1602
Malcolm Fridlund https://orcid.org/0000-0003-2180-9936
Keivan G. Stassun https://orcid.org/0000-0002-3481-9052
Coel Hellier https://orcid.org/0000-0002-3439-1439
Stephane Udry https://orcid.org/0000-0001-7576-6236
Michael Ireland https://orcid.org/0000-0002-6194-043X
Nicholas Law https://orcid.org/0000-0001-9380-6457
Andrés Jordán https://orcid.org/0000-0002-5389-3944
Néstor Espinoza https://orcid.org/0000-0001-9513-1449
Paula Sarkis https://orcid.org/0000-0001-8128-3126
David W. Latham https://orcid.org/0000-0001-9911-7388

References

Anderson, D. R., Collier Cameron, A., Hellier, C., et al. 2011, ApJL, 726, L19
Baraffe, I., Chabrier, G., Allard, F., & Hauschildt, P. H. 2002, A&A, 382, 563
Baraffe, I., Chabrier, G., Barman, T. S., Allard, F., & Hauschildt, P. H. 2003, A&A, 402, 701
Barragán, O., Gandolfi, D., & Antoniciello, G. 2019, MNRAS, 482, 1017
Bayliss, D., Gillen, E., Eigmüller, P., et al. 2018, MNRAS, 475, 4467
Bayliss, D., Hojjatpanah, S., Santerne, A., et al. 2017, AJ, 153, 15
Beatty, T. G., Morley, C. V., Curtis, J. L., et al. 2018, AJ, 156, 168
Bonomo, A. S., Sozzetti, A., Santerne, A., et al. 2015, A&A, 575, A85
Bouchy, F., Deleuil, M., Guillot, T., et al. 2011, A&A, 525, A68
Brahm, R., Jordán, A., & Espinoza, N. 2017a, PASP, 129, 034002
Brahm, R., Jordán, A., Hartman, J., & Bakos, G. 2017b, MNRAS, 467, 971
Brown, T. M., Baliber, N., Bianco, F. B., et al. 2013, PASP, 125, 1031
Burrows, A., Heng, K., & Nampaisarn, T. 2011, ApJ, 736, 47
Carmichael, T., Latham, D., & Vanderburg, A. 2019, AJ, 158, 38
Castelli, F., & Kurucz, R. L. 2004, arXiv:astro-ph/0405087
Chabrier, G., & Baraffe, I. 1997, A&A, 327, 1039
Choi, J., Dotter, A., Conroy, C., et al. 2016, ApJ, 823, 102
Collins, K. A., Kielkopf, J. F., Stassun, K. G., & Hessman, F. V. 2017, AJ, 153, 77
Csizmadia, S. & CoRot Team 2016, in The CoRoT Legacy Book: The Adventure of the Ultra High Precision Photometry from Space, ed. A. Baglin (Les Ulis: EDP Sciences), 143
Csizmadia, S., Hatzes, A., Gandolfi, D., et al. 2015, A&A, 584, A13
David, T. J., Hillenbrand, L. A., Gillen, E., et al. 2019, ApJ, 872, 161
Deleuil, M., Deeg, H. J., Alonso, R., et al. 2008, A&A, 491, 889
Díaz, R. F., Damiani, C., Deleuil, M., et al. 2013, A&A, 551, L9
Díaz, R. F., Montagnier, G., Leconte, J., et al. 2014, A&A, 572, A109
Donati, J.-F., Semel, M., Carter, B. D., Rees, D. E., & Collier Cameron, A. 1997, MNRAS, 291, 658
Dotter, A. 2016, ApJS, 222, 8
Eastman, J. D., Rodriguez, J. E., Agol, E., et al. 2019, arXiv:1907.09480
Gaia Collaboration, Brown, A. G. A., Vallenari, A., et al. 2018, A&A, 616, A1
Gillen, E., Hillenbrand, L. A., David, T. J., et al. 2017, ApJ, 849, 11
Gray, D. F. 2005, The Observation and Analysis of Stellar Photospheres (3rd ed.; Cambridge: Cambridge Univ. Press)
Hartman, J. D., Bayliss, D., Brahm, R., et al. 2015, AJ, 149, 166
Hodžić, V., Triaud, A. H. M. J., Anderson, D. R., et al. 2018, MNRAS, 481, 5091
Høg, E., Fabricius, C., Makarov, V. V., et al. 2000, A&A, 355, L27
Irwin, J., Buchhave, L., Berta, Z. K., et al. 2010, ApJ, 718, 1353
Irwin, J. M., Charbonneau, D., Esquerdo, G. A., et al. 2018, AJ, 156, 140
Jackman, J. A. G., Wheatley, P. J., Bayliss, D., et al. 2019, MNRAS, 489, 5146
Jackson, B., Greenberg, R., & Barnes, R. 2008, ApJ, 678, 1396
Jensen, E. 2013, Tapir: A Web Interface for Transit/Eclipse Observability, v1.0, Astrophysics Source Code Library, ascl:1306.007
Johnson, J. A., Apps, K., Gazak, J. Z., et al. 2011, ApJ, 730, 79
Johnson, J. A., Gazak, J. Z., Apps, K., et al. 2012, AJ, 143, 111
Kaufer, A., & Pasquini, L. 1998, Proc. SPIE, 3355, 844
Lightkurve Collaboration, Cardoso, J. V. d. M., Hedges, C., et al. 2018, Lightkurve: Kepler and TESS Time Series Analysis in Python, v1.0, Astrophysics Source Code Library, ascl:1812.013
Lindegren, L., Hernández, J., Bombrun, A., et al. 2018, A&A, 616, A2
Mandel, K., & Agol, E. 2002, ApJL, 580, L171
Marcy, G. W., & Butler, R. P. 2000, PASP, 112, 137
Masuda, K., & Winn, J. N. 2020, AJ, 159, 81
Mazeh, T. 2008, EAS, 29, 1
Meibom, S., & Mathieu, R. D. 2005, ApJ, 620, 970
Milliman, K. E., Mathieu, R. D., Geller, A. M., et al. 2014, AJ, 148, 38
Moutou, C., Bonomo, A. S., Bruno, G., et al. 2013, A&A, 558, L6
Nowak, G., Palle, E., Gandolfi, D., et al. 2017, AJ, 153, 131
Paxton, B., Marchant, P., Schwab, J., et al. 2015, ApJS, 220, 15
Pepe, F., Mayor, M., Rupprecht, G., et al. 2002, Msngr, 110, 9
Persson, C. M., Csizmadia, S., Mustill, A. e. J., et al. 2019, A&A, 628, A64
Queloz, D., Mayor, M., Udry, S., et al. 2001, Msngr, 105, 1
Quinn, S. N., & White, R. J. 2016, ApJ, 833, 173
Saumon, D., & Marley, M. S. 2008, ApJ, 689, 1327
Siverd, R. J., Beatty, T. G., Pepper, J., et al. 2012, ApJ, 761, 123
Skrutskie, M. F., Cutri, R. M., Stiening, R., et al. 2006, AJ, 131, 1163
Smith, J. C., Stumpe, M. C., Van Cleve, J. E., et al. 2012, PASP, 124, 1000
Spiegel, D. S., Burrows, A., & Milsom, J. A. 2011, ApJ, 727, 57
Stassun, K. G., Collins, K. A., & Gaudi, B. S. 2017, AJ, 153, 136
Stassun, K. G., Corsaro, E., Pepper, J. A., & Gaudi, B. S. 2018a, AJ, 155, 22
Stassun, K. G., Mathieu, R. D., & Valenti, J. A. 2006, Natur, 440, 311
Stassun, K. G., Oelkers, R. J., Pepper, J., et al. 2018b, AJ, 156, 102
Stassun, K. G., & Torres, G. 2016, ApJL, 831, L6
Stumpe, M. C., Smith, J. C., Catanzarite, J. H., et al. 2014, PASP, 126, 100
Subjak, J., Sharma, R., Carmichael, T. W., et al. 2020, AJ, 159, 151
Tokovinin, A. 2018, PASP, 130, 035002
Tokovinin, A., Fischer, D. A., Bonati, M., et al. 2013, PASP, 125, 1336
Triaud, A. H. M. J., Gillon, M., Ehrenreich, D., et al. 2015, MNRAS, 450, 2279
Wright, E. L., Eisenhardt, P. R. M., Mainzer, A. K., et al. 2010, AJ, 140, 1868
Yee, S. W., Petigura, E. A., & von Braun, K. 2017, ApJ, 836, 77
Zhou, G., Bakos, G. Á, Bayliss, D., et al. 2019, AJ, 157, 31
Zhou, G., Bayliss, D., Hartman, J. D., et al. 2014, MNRAS, 437, 2831
Ziegler, C., Tokovinin, A., Briceno, C., et al. 2020, AJ, 159, 19